AGU PUBLICATIONS

JGR

Journal of Geophysical Research: Solid Earth

RESEARCH ARTICLE
10.1002/2015JB012786

Key Points:
- Seismic moulin tremor observed on the Greenland Ice Sheet
- Seismoacoustic resonance in a moulin shaft triggered by the waterfall hitting the water surface
- Modeling of the seismic wavefield depending on moulin geometry and two different source types

Supporting Information:
- Supporting Information S1

Correspondence to:
C. Roeoesli,
claudia.roeoesli@alumni.ethz.ch

Citation:
Roeoesli, C., F. Walter, J.-P. Ampuero, and E. Kissling (2016), Seismic moulin tremor, *J. Geophys. Res. Solid Earth*, *121*, 5838–5858, doi:10.1002/2015JB012786.

Received 2 JAN 2016
Accepted 10 JUL 2016
Accepted article online 13 JUL 2016
Published online 8 AUG 2016

Seismic moulin tremor

Claudia Roeoesli[1,2,3], Fabian Walter[1,2,3], Jean-Paul Ampuero[4], and Edi Kissling[1]

[1]Institute of Geophysics, ETH Zürich, Zürich, Switzerland, [2]Laboratory of Hydraulics, Hydrology and Glaciology (VAW), ETH Zürich, Zürich, Switzerland, [3]Swiss Seismological Service (SED), ETH Zürich, Zürich, Switzerland, [4]Seismological Laboratory, California Institute of Technology, Pasadena, California, USA

Abstract Through glacial moulins, meltwater is routed from the glacier surface to its base. Moulins are a main feature feeding subglacial drainage systems and thus influencing basal motion and ice dynamics, but their geometry remains poorly known. Here we show that analysis of the seismic wavefield generated by water falling into a moulin can help constrain its geometry. We present modeling results of hour-long seimic tremors emitted from a vertical moulin shaft, observed with a seismometer array installed at the surface of the Greenland Ice Sheet. The tremor was triggered when the moulin water level exceeded a certain height, which we associate with the threshold for the waterfall to hit directly the surface of the moulin water column. The amplitude of the tremor signal changed over each tremor episode, in close relation to the amount of inflowing water. The tremor spectrum features multiple prominent peaks, whose characteristic frequencies are distributed like the resonant modes of a semiopen organ pipe and were found to depend on the moulin water level, consistent with a source composed of resonant tube waves (water pressure waves coupled to elastic deformation of the moulin walls) along the water-filled moulin pipe. Analysis of surface particle motions lends further support to this interpretation. The seismic wavefield was modeled as a superposition of sustained wave radiation by pressure sources on the side walls and at the bottom of the moulin. The former was found to dominate the wave field at close distance and the latter at large distance to the moulin.

1. Introduction

For a better understanding of recent glacier mass balance changes, and thus global sea level rise, the impact of a warming climate on enhanced meltwater production and its feedback with increasing glacier and ice sheet velocities have come recently into focus in glacial research [e.g., *Rignot et al.*, 2011; *Box and Colgan*, 2013]. The characteristics and evolution of the glacial drainage system are crucial components of glacier dynamics due to their direct influence on basal motion [e.g., *Zwally et al.*, 2002; *Bell*, 2008; *Harper et al.*, 2010; *Bartholomew et al.*, 2012]. Glacial drainage systems are complex networks that may consist of cavities, conduits, and fractures at the glacier bed [*Iken*, 1981; *Iken and Bindschadler*, 1986; *Fountain et al.*, 2005; *Gulley et al.*, 2009] undergoing strong changes during a season [e.g., *Sundal et al.*, 2011; *Andrews et al.*, 2014]. The development of the drainage system from a pressurized distributed system to a low-pressure channelized system controls the impact of changes in meltwater input to (local) basal water pressure [e.g., *Bartholomew et al.*, 2010; *Chandler et al.*, 2013]. Thus, the characteristics and capacity of the drainage system defines the influence of (peak) meltwater input on basal motion [e.g., *Bartholomew et al.*, 2012; *Andrews et al.*, 2014; *Carmichael et al.*, 2015].

The main pathways routing meltwater to the glacier base are moulins, vertical shafts fed by surface streams that constitute efficient hydraulic connections to the glacier bed. Moulins deliver large amounts of meltwater to the glacier bed at discrete points and change the subglacial water pressure on diurnal and seasonal time scales [*Gulley et al.*, 2012; *Andrews et al.*, 2014]. Moulins are presumed to form from hydrofracturing of water-filled crevasses or surface lakes [*van der Veen*, 2007; *Das et al.*, 2008; *Benn et al.*, 2009] and exist in ablation zones built through cold ice, possibly through more than 1 km thick ice. Moulins often form at fixed geographical locations controlled by the subglacial bedrock topography and can be active for several years [*Catania and Neumann*, 2010]. The shape of the moulin conduit and its changes due to continuous meltwater flow are barely known and difficult to investigate [e.g., *Holmlund*, 1988; *Gulley et al.*, 2009]. The assumption of a vertical shaft directly connected to the ice sheet bed might be valid only at first order; moulins are expected to

have complex geometries [*Reynauld*, 1986; *Holmlund*, 1988; *Schroeder*, 1998; *Vatne*, 2001; *Catania et al.*, 2008], possibly consisting of a series of shafts with subsequent plunge pools and cavities [*Holmlund*, 1988; *Gulley et al.*, 2009].

As shown by *Röösli et al.* [2014], the large amounts of meltwater draining through a moulin can generate vibrations that can be measured as ground displacement by seismic sensors. This seismic signal dominates other sources of microseismic energy at the study site on the Greenland Ice Sheet, as shown by reliable epicentral location analysis. The occurrence, duration, and frequency content of the seismic signal was found to correlate with the water level measured in the same moulin. The moulin seismic signal was sustained over long durations of several hours and characterized by gliding spectral peaks and an emergent onset with no clear *P* and *S* wave phase arrivals. These characteristics are similar to those of harmonic volcanic tremors [*Chouet*, 1996; *Chouet and Matoza*, 2013], a phenomenon regularly observed in active volcanos and with a long history in volcano seismology research [e.g., *Minakami*, 1974; *Aki et al.*, 1977].

Chouet [1985] analyzed volcanic tremors and introduced a model of vertical cylindrical pipe filled with fluid magma in which waves excited by a triggering mechanism resonate. The interaction of the pressure waves in the magma with the elastic deformation of the solid walls of the magma conduit leads to so-called tube waves. These tube waves propagate along the conduit and resonate due to its finite length, hence emitting seismic energy with sharp spectral peaks. *Chouet* [1985] pointed out that to understand the detailed processes, the resonance effects need to be separated from other effects such as excitation and propagation [*Lesage et al.*, 2002]. This model of a vertical cylindric fluid-filled pipe is analogous to a moulin shaft filled with water.

The analogy of fluid-related seismic sources in glaciers and volcanoes is not new: emergent and sustained tremor seismograms associated with water propagation have been reported under the Antarctic Ice Sheet [*Winberry and Anandakrishnan*, 2009] and nonpolar mountain glaciers [*Heeszel et al.*, 2014; *Bartholomaus et al.*, 2015]. *Lawrence and Qamar* [1979] suggested that fluid-filled fractures cause resonance effects in volcanoes and glaciers. Several subsequent studies have shown that water resonances triggered by fracturing in glacier ice are a common phenomenon in high melt areas [*Métaxian et al.*, 2003; *West et al.*, 2010; *Röösli et al.*, 2014] and that temporal changes in resonance peaks may reflect geometric changes associated with fracture tip propagation [*Heeszel et al.*, 2014; *Helmstetter et al.*, 2015]. Considering recent advances in theoretical treatments of guided waves in englacial fractures [*Dunham and Ogden*, 2012; *Lipovsky and Dunham*, 2015], these findings suggest that seismology is well suited to monitor subsurface water drainage in glaciers and ice sheets.

This study focuses on water resonances within a major englacial drainage channel. We investigated and modeled different components of seismic moulin tremors observed on the Greenland Ice Sheet to define a first-order physical model of the tremor source. Our model consists of the inflowing water acting as excitation of acoustic waves in the water-filled, cylindric shaft, which then acts as a resonator. We combined observations of tremor amplitude, frequency content. and three-component particle motion to constrain model parameters related to moulin geometry and its evolution during the 42 day observation period. In particular, we were able to model the characteristic frequencies of the moulin tremor using a semiopen organ pipe resonance model. The modeling constrained the bottom of the resonator to about 180 m below surface, corresponding to around 30% of the ice thickness. Furthermore, we modeled the tremor source as a combination of a bottom source (water column interacting with the bottom of the resonator) and a cylindric source (water column interacting with the conduit walls) and constrained their relative contribution using the orientation of the particle motion ellipses. Thus, we were able to observe and monitor the englacial interaction between large amounts of meltwater and the ice sheet generating the seismic tremor.

2. Observation Network and Study Site

Our study is based on data from a seismic network that operated in July and August 2011 in the ablation zone of the western Greenland Ice Sheet. It consisted of seismometers (Figure 1a) installed on the ice surface and in boreholes. The core network comprised nine Lennartz LE-3D seismometers (FX01–FX09) installed inside an 800 m circular configuration. Three additional shallow borehole seismometers (2–3 m depth, Lennartz LE-3D/BH, FX10–FX12) enlarged the aperture of the network. Unfortunately, station FX11 suffered an early outage and could not be used for most of the analysis. All seismometers have a flat response between 1 and 80 Hz. Each seismometer was equipped with a Nanometrics' Taurus digitizer, continuously recording at 500 Hz sampling frequency.

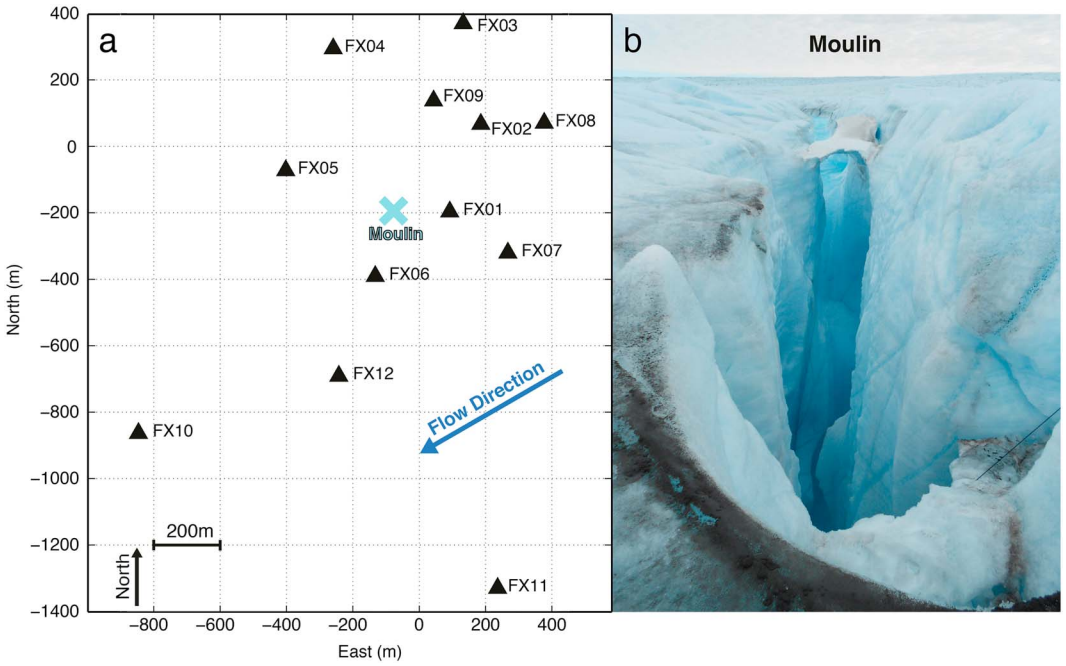

Figure 1. (a) Map of the seismometer network (black triangles) with the moulin in the center (blue cross). (b) Moulin with inflowing stream and small snow bridge. The stream feeding the moulin is about 1.25 m wide. Picture was taken on 8 August 2011 (Andreas Bauder), shortly before the collapse of the snow bridge.

A large moulin (Figure 1b) with an opening diameter at the surface of approximately 5–10 m was located inside the core network and was fed by a surface stream with up to 5 m^3 s^{-1} peak water discharge. On average, the stream drained 2–3 m^3 s^{-1} of water with large daily variations but never dried completely [*Röösli et al.*, 2014]. The water level of the stream was monitored, but due to fast changes of the stream bed shape, discharge estimates were poorly constrained.

The moulin was equipped with a pressure sensor measuring the water level. As the sensor was installed 163 m below the ice surface, we were unable to measure water levels lower than 163 m, which created data gaps mostly in the morning hours and the daily minima were unknown. Nevertheless, the water level rose almost daily above the pressure sensor and showed strong diurnal variations. The variations in water level in a moulin depend on amount of inflowing water, capacity of the subglacial drainage system (outflowing water), and moulin geometry [*Andrews et al.*, 2014] and are difficult to assess. Additional observations obtained during the comprehensive glaciological campaign covered various aspects of the glacial dynamics and can also be found in *Röösli et al.* [2014] and *Ryser et al.* [2014a].

3. General Tremor Characteristics

During the seismic campaign, the seismometers recorded strong tremor activity most of the days. The tremors lasted from 4 to 16 h, with an average duration of 6 h (Figure 2 and supporting information Figure S1). The glacial tremor was characterized by a rather abrupt onset but no distinct *P* or *S* wave arrivals, which is a well known characteristic of emergent volcanic tremors [e.g., *Chouet*, 1996]. Therefore, location techniques based on wave arrival times, as routinely applied for earthquake location [e.g., *Lomax et al.*, 2000], could not be used. Instead, the source location was determined by the decay of tremor amplitude versus distance to the source across the seismic network by *Röösli et al.* [2014]. The tremor source was located in the vicinity of the large, central moulin inside the seismic network (Figure 1a, blue cross). The frequency content of this "moulin tremor" showed strong correlation with the moulin water level [*Röösli et al.*, 2014]. It was therefore hypothesized that the tremor is caused by meltwater flowing into this englacial channel.

In order to visualize the main tremor characteristics, spectrograms highlight the distribution of energy as a function of time and frequency (Figure 2). Spectrograms were processed using a moving window of 32.8 s and an overlap of 80%, chosen empirically based on the trade-off between temporal and frequency resolution.

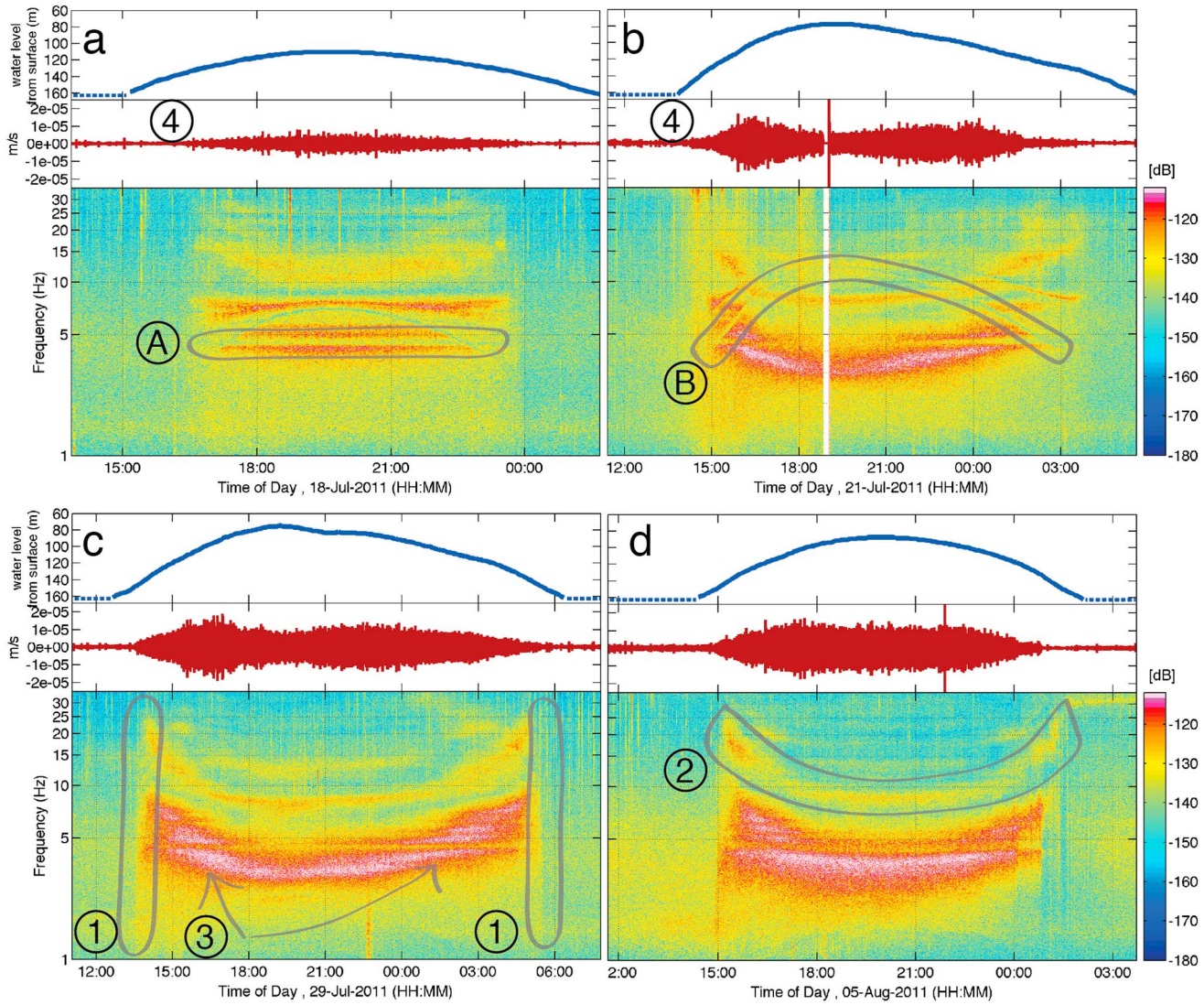

Figure 2. (a–d) Spectrograms (bottom panels) for four tremor episodes with filtered waveforms (2–11 Hz, middle panels) and the concurrent water level measured inside the moulin drawn as distance from surface (top panels, dashed line denotes times when the water level was below sensor). Numbers label main characteristics of the moulin tremor: (1) abrupt beginning and end; (2) 2–3 visible "thick" bands of energy (middle one is labeled). The third band is best visible in spectrogram C; and (3) changes in amplitude of the emitted seismic energy; (4) cigar-shaped filtered waveform. Second-order characteristics: (A) constant and horizontal bandgaps with lack of energy and (B) small bandgap correlating with the water level inside the moulin (top panels). All records are from station FX01.

Figure 2 shows spectrograms of four tremor episodes with varying duration recorded by station FX01 (Figure 1). In Figure S1, the time series for the entire observation period for stations FX01 and FX06 are shown. For the different seismic stations, the overall pattern in the spectrograms is coherent and we, therefore, inferred that the same source generated the seismic signals.

A striking feature in the spectrogram and filtered (Butterworth, two-pole, 2–11 Hz) waveforms is the abrupt start of maximal energy density (Figure 2, label 1) and its U-shaped change in frequency content during each tremor episode (label 2). A systematic change in amplitude over time is indicated by the changes in color (pink is high energy, Figure 2, label 3) and by the amplitude of the filtered waveform in the middle panel (Figure 2, label 4). Second-order effects, not investigated in this paper, include horizontal bands of absorbed energy (label A in Figure 2), hereafter called "bandgaps," and very thin, gliding bands of absorbed energy in some tremor episodes (label B in Figures 2a and 2b). Initially one, and later in the season two gliding thin absorption bands (Figures 2a and 2b, respectively) with frequency dependent on moulin water level (Figure 2, top panels) were observed from 4 July to 30 July 2011 (Figures 2c and 2d and S2). Both types of energy

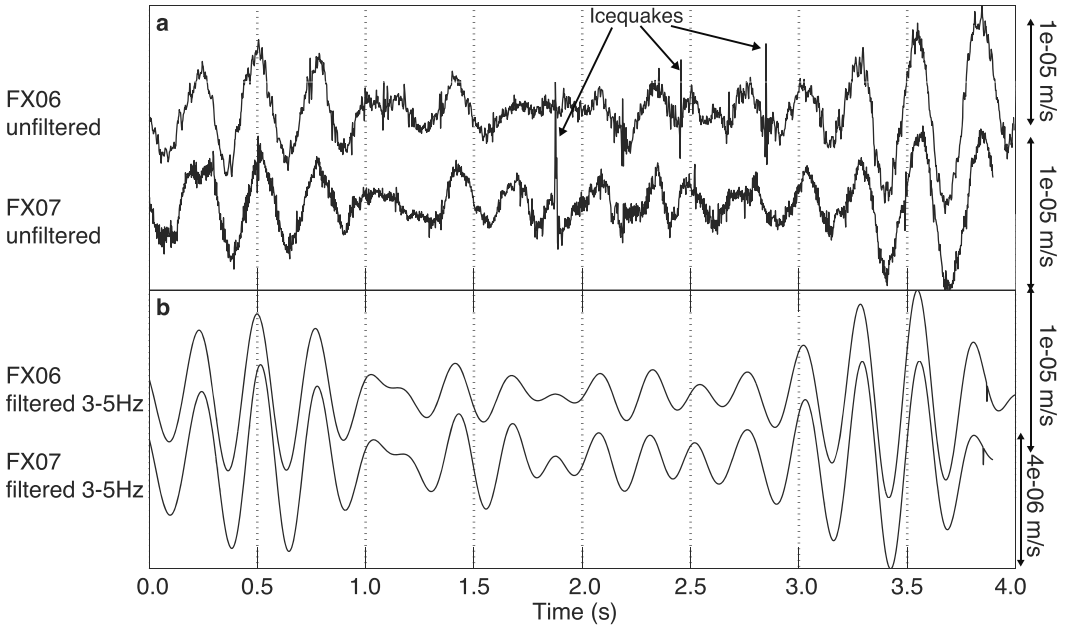

Figure 3. Seismic waveform (vertical component) observed during a tremor episode with stations FX06 and FX07, installed in 205 m and 377 m distance from the source, respectively. The high waveform similarity demonstrates the coherency of the seismic signal measured on different seismic stations. (a) Unfiltered and aligned waveforms with the moulin tremor (low frequency) superimposed by high-frequency noise and local high-frequency icequakes (marked with the arrows). (b) Filtered waveform (shown in Figure 3a, two-pole Butterworth filtered between 3 and 5 Hz), emphasizing the coherency of the moulin tremor.

absorption bands, horizontal and "gliding," were measured on all seismic stations; thus, these features were source related.

Röösli et al. [2014] and *Walter et al.* [2015a] showed that the moulin tremor was characterized by a high level of coherency and dominated the signals observed within the seismometer network between 3 and 5 Hz. Figure 3a shows unfiltered waveforms for stations FX06 and FX07 located at 205 m and 377 m distance from the moulin, respectively. Waveforms are aligned to account for different arrival times. Both waveforms are dominated by the low-frequency tremor (with different amplitudes) overlaid with high-frequency noise and spiky signals from high-frequency local icequakes [*Röösli et al.*, 2014] (Figure 3, marked with arrows). Filtering the waveform between 3 and 5 Hz (Figure 3b, two-pole Butterworth filtered) enhances the coherent waveform pattern and emphasizes the high similarity.

The Fourier spectra shown in Figure 4 illustrate the typical distribution of energy in different frequency ranges at the beginning of a tremor episode. The power spectrum density (PSD, *y* axis) of seven stations installed at different distances from the source was calculated from a 2 h recording of the vertical component for frequencies between 2 and 11 Hz (Figure 4, ordered by increasing station distances from a to g). Multiple spectral maxima are observed at similar frequencies at all stations. The relative peak amplitudes, however, are different. For the two closest stations (Figures 4a and 4b) and the farthest station (FX10, Figure 4g), the lower three energy peaks at 4.1, 4.9, and 5.6 Hz have higher amplitude than the upper two maxima at 6.3 and 7.2 Hz. For stations at intermediate distance of 500–600 m (Figures 4e and 4f), the lowest energy peak of 4.1 Hz is weaker than the second and third peaks. The different relative peak amplitudes are possibly caused by the different attenuation characteristics of different wave types, for instance, a faster attenuation of body waves (distance^{-1}) than surface waves (distance$^{-\frac{1}{2}}$), by an asymmetric radiation pattern [*Lay and Wallace*, 1995], or by site effects.

4. Source Model

To propose a physical source model, we build upon experience gained in volcano seismology. *Chouet* [1985] investigated seismic long-period volcanic events and developed a model of buried, vertical fluid-filled pipe. He modeled the source of harmonic volcanic tremors as the resonance of tube waves (fluid-solid

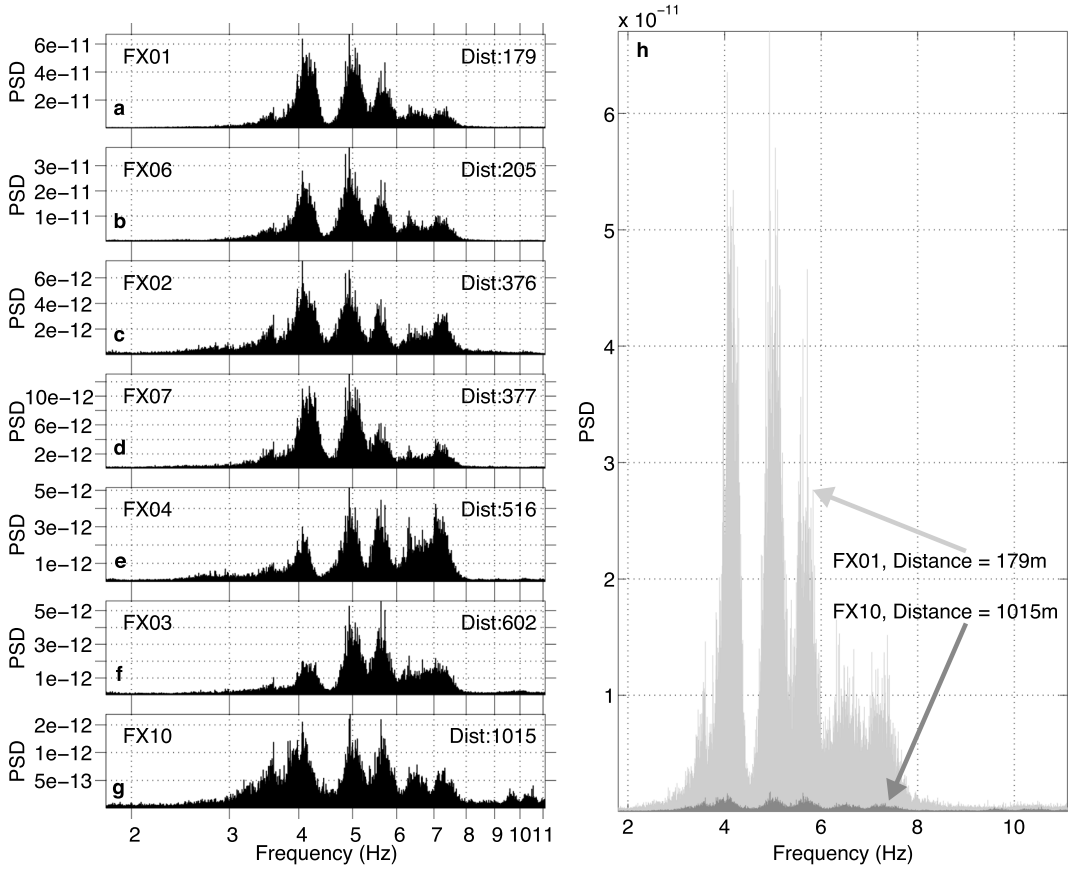

Figure 4. (a–g) Fast Fourier analysis for a 2 h window of tremor episode measured on seven stations installed in different distances from the moulin (ascending from top). Frequency content between 2 and 11 Hz is dominated by bandgaps and a changing relative distribution of the energy between the individual peaks per station. Note, even for FX10 individual peaks are visible. (h) Analogue to Figures 4a and 4g thus with same *y* axis scale.

interface-guided waves with wavelength much larger than the pipe radius) along a magma-filled volcanic pipe, triggered by excess gas pressure. His model consists of a cylindrical pipe, a circular disk shutting off its bottom, and an open surface at the top (trigger location).

Our analogous model for moulin tremors is shown in Figure 5 with the water-filled, vertical moulin shaft as fluid-filled pipe interacting with the solid ice walls, and a water fall hitting the water surface as trigger. We observed moulin tremors only when the moulin water level rose above a certain value. We interpret this threshold behavior as follows: If the waterfall jet impinges directly on the water surface, it efficiently excites water acoustic waves and leads to seismic moulin tremors. If the water jet impinges on the moulin ice walls or on a plunge pool, no moulin tremor is excited. The water level threshold for tremor onset is hence interpreted as arising from the morphology of the moulin. Particular to our system is the continuous triggering of the seismic signal by the surface stream continuously feeding the moulin system. This sustained source generates the hour-long, continuous tremor signal.

Similar to the magma-filled cylinder model of *Chouet* [1985], the moulin is filled with water acting as a resonating body that concentrates the acoustic energy radiated by the waterfall in specific frequency bands. The coupling of water acoustic pressure and elastic deformation of the moulin walls generates waves along the moulin known as tube waves. Because of the finite height of the moulin, these tube waves resonate. Their energy is then radiated into the ice as seismic waves. The frequency content of the source of seismic waves is determined by resonant modes analogous to those of a semiopen organ pipe. Their resonance frequencies are controlled by the height of the water column. The moulin geometry may be constricted at the bottom by a kink. If this geometrical restriction induces significant change of impedance for tube waves, then it constitutes an effective end of the resonant body. In our simple model, we assume that the cylindrical,

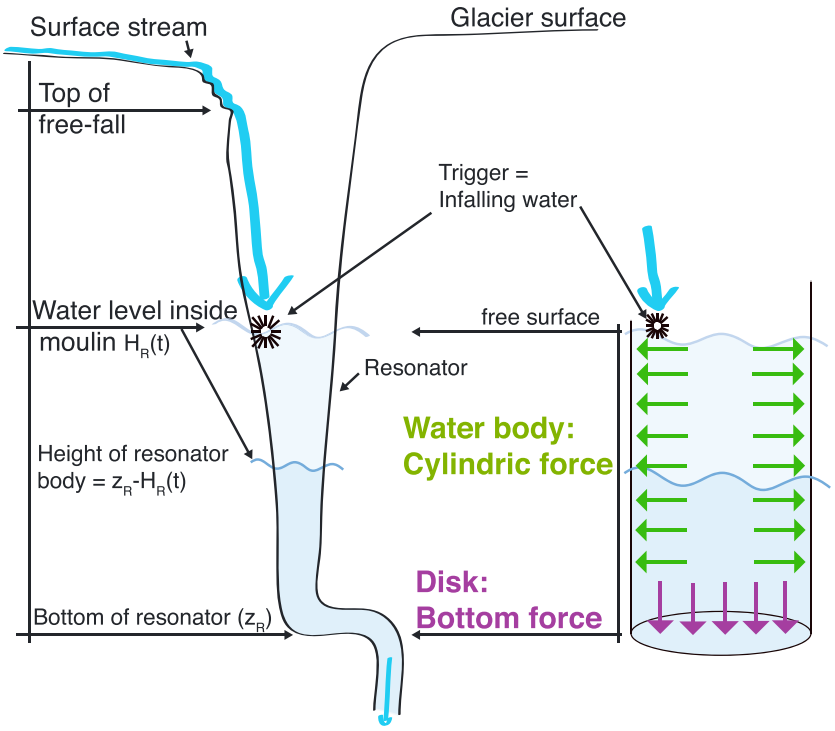

Figure 5. Source Model of the moulin tremor with trigger and resonator body, changing height depending on the moulin water level. We propose that the waves are generated by the interference of two different types of sources: A cylindric source caused by the interaction of the water column with the solid ice walls and a bottom source caused by the interaction of the water column with the bottom of the resonator.

vertical moulin pipe is effectively closed for tube waves at the bottom (Figure 5). Because tube waves have wavelengths much larger than the moulin cross section, the moulin bottom can be closed for tube waves but open for water flow.

The model predicts a systematic variation of the particle motion of tremor signals as a function of distance from the moulin and of moulin water level. The seismic signal was a combination of waves generated by two source types: the deformation of the moulin walls induced by tube waves, hereafter called cylindric source (Figure 5, green), and the diffraction of waves at the bottom of the resonance body, hereafter called bottom source (Figure 5, purple). *Chouet* [1985] demonstrated that energy emitted by the cylindric source dominates near- and intermediate-field seismic waves, whereas the bottom source attenuates less rapidly with distance and dominates the far field.

4.1. Triggering of Moulin Tremor

The moulin tremor was solely active when the water level inside the moulin rose several meters higher than the pressure sensor (installed at about 163 m below surface, Text S2), and its energy was observed mostly in frequencies below 11 Hz (Figure 2). The beginning and end of the tremor episodes were defined by sudden changes of coherency between waveforms (Figure S2). Coherency was quantified by the cross-correlation coefficient between waveforms recorded by several station pairs, computed on a sliding window. To quantify the strength of the tremor, we calculated the power recorded by the station closest to the moulin, FX01, by integrating the PSD between 3 and 11 Hz on 32.8 s long sliding windows. We compared the tremor power (green curve in Figures 6a and 6b) with the water flux, represented by the water height of the surface stream (Figure 6a, dark blue), and with the moulin water level (Figure 6b, light blue). The energy emitted by the tremor has maximum values (light green bands) near the beginning of a moulin tremor episode and a continuous decay over the duration of the tremor.

This qualitative comparison of the tremor amplitude with the water level of the surface stream (Figure 6a) and the moulin water level (Figure 6b) reveals that maximum tremor amplitudes (black arrows in Figure 6a) better match the daily peaks of stream water height than the peaks of moulin water level. The maximum moulin water level typically occurs several hours after the maxima of stream water level and tremor amplitude and

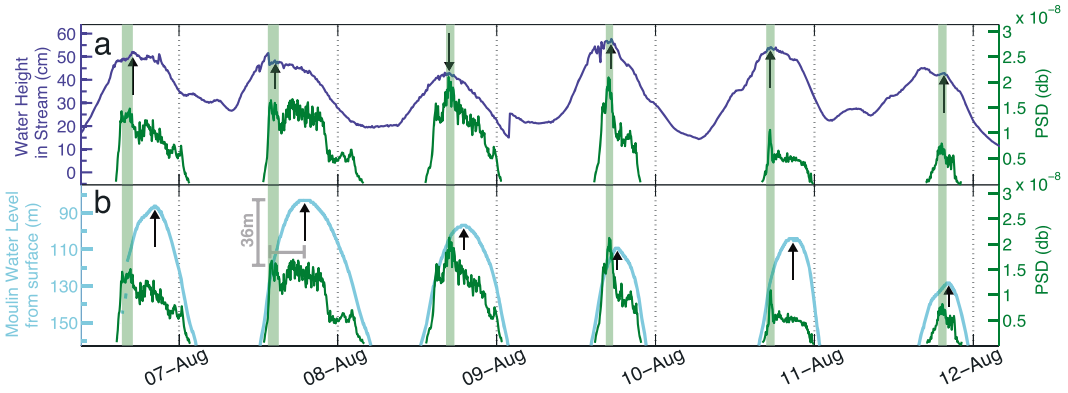

Figure 6. Time series of 6 days of observation with (a) the water level of the surface stream (dark blue line) and (b) the moulin water level (light blue line) in comparison to the integrated energy of the moulin tremor (dark green lines). The light green vertical bars mark maxima in observed energy and are in phase with the stream water level (Figure 6a) and earlier to the maxima in moulin water level (Figure 6b). Grey lines in Figure 6b mark changes in moulin water level (vertical bar) of 36 m, while tremor amplitude (horizontal bar) is not accordingly changing.

varies for different tremor episodes. This aspect is especially visible on 8 August 2011 (second tremor in the time series in Figure 6b): a constant (or even decreasing) tremor energy coincided with a small decrease in stream water level and with a 36 m rise in moulin water level (marked with grey bars in Figure 6b), almost half of the entire change in the moulin water level during this tremor episode.

We therefore conclude that at first order, the energy of the moulin tremor is controlled by the inflowing water rather than by the water level inside the moulin and the peaks in moulin tremor energy correspond to a high stream discharge into the moulin. Thus, the changing moulin water level and the corresponding change in height of water fall influences the moulin tremor energy at most in second order. Furthermore, short-term fluctuations in tremor energy may be caused by second-order effects such as energy absorption at particular frequencies. For instance, the sudden drop in tremor energy between grey bars marked in Figure 6b might be caused by the absorption of energy within the horizontal bandgaps labeled with a in Figure 2.

4.2. Changing Frequency Content of Moulin Tremors

Röösli et al. [2014] already reported the strong correlation between the moulin tremor properties and moulin water level. The spectrograms in Figure 2 show this correlation: energy is enhanced at higher frequencies when moulin water level is lower and vice versa. We observed two to three individual bands of energy, with most of the energy emitted between 3 and 11 Hz. These separated frequency bands are an indication for a resonance model in which the excited seismic energy is concentrated in frequency bands that depend on the height and cross-section geometry of the resonator. Thus, the frequency distribution of the radiated seismic signal is controlled by the changing moulin water level, which controls the height of the resonant body. The first overtone of the excited resonance is labeled number 2 in Figure 2d. The next overtone is only visible during strong tremors (e.g., Figure 2c) and has higher energy at the beginning and end of the tremors (red color).

4.2.1. Resonance Model of a Cylindrical Water-Filled Pipe

Following *Chouet* [1985], we modeled the different bands of energy as the resonance modes of a cylindrical water-filled pipe analogous to the organ pipe model (semiopen). The frequency of the *n*th mode is predicted to depend on moulin water level [*Chouet*, 1985] as

$$f_n(t) = \frac{n}{4}\frac{c_R}{D(t)}, \quad n = 1, 3, 5, \ldots \tag{1}$$

where $D(t) = z_R - H_R(t)$ denotes the resonating water column at time t, $H_R(t)$ the measured water level depth, and z_R the unknown bottom depth of the resonator. The latter is assumed to be constant over the duration of each tremor episode. Furthermore, c_R denotes the velocity of tube waves. Tube waves are acoustic waves in the water whose pressure perturbations are coupled to quasi-static elastic deformation of the conduit walls (elasticity of the surrounding ice, *Chouet* [1985]). Their speed depends on the geometry of the conduit cross section. As a first-order assumption, we assume that the cross section is the same at all depths and can be

represented by its ellipticity α, defined as the ratio between the two principal axes of the ellipse (for a circular cross section, $\alpha = 1$). Ellipticity α is the second unknown parameter that was estimated within the modeling procedure. Combining results by *Biot* [1956], *Chouet* [1985], and *Norris* [1990], we obtained the following compact expression for c_R:

$$c_R = \left(\frac{b/\rho}{1 + (b/\mu) \cdot X} \right)^{1/2}, \tag{2}$$

with

$$X = 1 + \frac{(1-\nu)(1-\alpha)^2}{\alpha}, \tag{3}$$

where b the bulk modulus of water, ρ the density of water, μ the shear modulus of ice, and ν the Poisson ratio of ice. We used $b = 1.98$ GPa and $\rho = 999.9$ kg m^{-3} for water at 0°, $\mu = 3.5 \times 10^9$ N m^{-2}, and $\nu = 0.31$ [*Petrenko and Whitworth*, 1999].

The semiopen resonator model predicts a sequence of fundamental, first and second overtones frequencies proportional to 1, 3, 5. This is reasonably verified in the moulin tremor spectrograms: the ratio f_5/f_3 is close to 5/3, while f_3/f_1 is somewhat lower than 3. Departures from the simplified model adopted here can be due, for instance, to a finite impedance at the top and bottom of the resonator.

4.2.2. Observation and Inversion for Model Parameters

Due to the complex spectrum of the fundamental mode (Figure 4), we used the better defined first higher mode for modeling. We extracted the frequency of maximum PSD at frequencies higher than the fundamental mode from the spectrogram of the closest station from the moulin, FX01, in each sliding time window. Figure 7a shows in colored circles the extracted frequencies (y axis) of the first higher mode ($n = 3$) for the moulin tremor observed on 8 August 2011 (Figure 7b). The frequency content is compared with the concurrent moulin water level (x axis, Figure 7a), and different colors denote the duration since the beginning of the tremor. We observe a symmetric course without hysteresis (colored points in Figure 7a), supporting the assumption that the frequency content is independent from the trigger and that the moulin geometry (α and z_R) is constant over the duration of a tremor episode. The extraction of the overtone frequency is complicated by the presence of absorption bands in the spectra, or other features that do not anticorrelate with water level, and tremors of low signal-to-noise ratio (SNR).

We inverted for α and z_R using Matlab's robust bisquare fitting algorithm following equations (1) to (3) and obtained $\alpha = 0.379 \pm 0.015$ and $z_R = 181.8 \pm 0.8$ m with a fit quality R^2 of 0.94 (red curve, Figure 7a). The uncertainty boundaries were calculated with a 0.99% confidence interval for the fitting procedure and consider only the quality of the fitted points. The true uncertainty is strongly underestimated because the point cloud extraction, changes in SNR, coupling of the parameters, and the influence of the frequency bandgaps are not included and difficult to assess. The highly scattered estimated frequencies corresponding to moulin water head >140 m (grey points in Figure 7a) were excluded from the fitting procedure. These data points resulted from the different onset in high energy for the frequency band >11 Hz (first higher mode) in comparison with the frequency range of 3–5 Hz used for tremor picking (Text S2 and Figure 7b). The three harmonics (red curves, spectrogram Figure 7b) are drawn with equation (1) using values for α and z_R estimated in the example shown in Figure 7a (red curve) and with the n values corresponding to each mode.

4.2.3. Evolution of Moulin Geometry

Changes in α and z_R estimated for each tremor episode reflect changes in moulin geometry. However, these two parameters trade off significantly. A higher α and lower z_R result in shifting the fitted curve (Figure 7a, red line) toward higher frequencies. Furthermore, changes in z_R value affect the curvature (lower z_R results in a steeper curve). This trade-off, together with low SNR and frequency band gaps, makes the fitting procedure for the majority of the tremor episode unstable. A classical parameter estimation and uncertainty estimation via goodness of fit or bootstrapping is therefore not sufficient to verify if there are physical changes in the resonator geometry.

Instead, we tested the hypothesis that none of the parameters changes between successive moulin tremors and that the differences in inversion results for different tremor episodes are caused by the fitting procedure. We adopted as reference scenarios the estimated parameters of two tremors with highest SNR (28 July and 8 August 2011). Assuming a constant α given by the value estimated for the tremor of either 28 July (Figure 7c1, green triangle) or 8 August (Figure 7c1, blue triangle), we inverted for z_R on each of the remaining days of

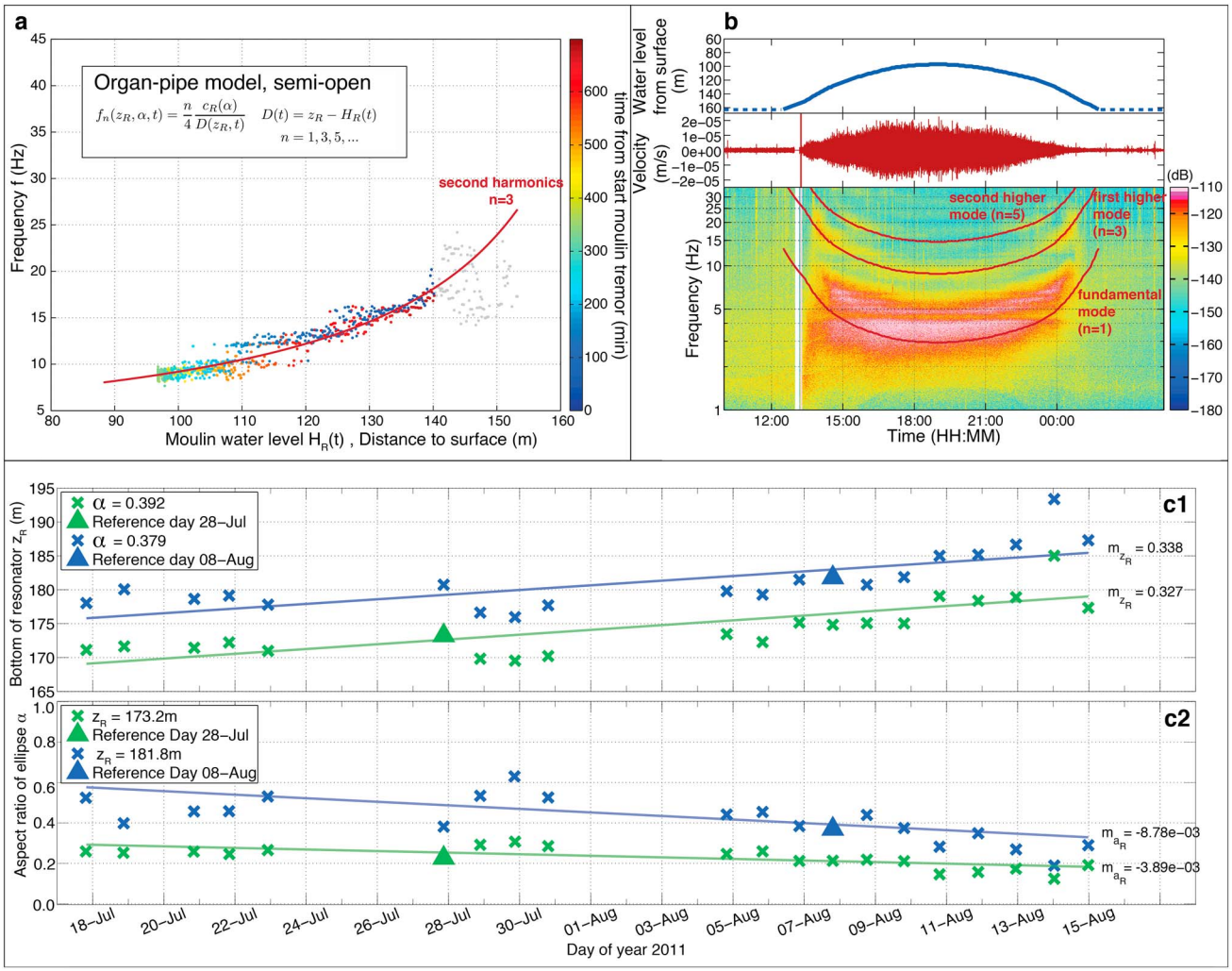

Figure 7. Modeling of the resonance of seismoacoustic waves in a semiopen organ pipe applied to observations and the test of evolution of the resonator geometry during the season. (a) Extracted frequency content of the first higher mode (points) with the least square robust fit (red curve) using the equation for an organ pipe model. Colored points denote time of observation from the tremor beginning. The grey points were not used for the fitting procedure. (b) Spectrogram with harmonic frequencies (red) calculated for the fundamental mode and two overtones with α and z_R estimated with the curve shown in Figure 7a. Testing of the hypothesis that the resonator configuration of the moulin was constant during the season with α (accounting for variability in cross section of the cylinder) and z_R (bottom depth of the resonator) being constant. (c1) Two reference scenarios (green and blue triangles, respectively) with fixed α used for estimating the corresponding z_R per tremor episode (crosses). (c2) Same scenario as for c1, however, with z_R fixed and the inversion calculated for α. There is the same trend for all test scenarios; thus, the hypothesis of a constant resonator configuration is rejected. The moulin evolves during the season toward higher complexity (lower α) and/or lower bottom of the resonator (higher z_R).

tremor. We expect a constant z_R if the α value is correct and resonator cross-section geometry is constant. The robustness of our hypothesis was tested by also calculating the opposite scenario, assuming a fixed z_R and inverting for α (Figure 7c2).

Both test cases of fixed ellipticity α (Figure 7c1) resulted in the same trend of increasing z_R value by about 9 m over 29 days (Figure 7c1) with a R^2 of about 0.3–0.5. The difference between the two scenarios per tremor episode is in average 7 m, with a standard deviation of 1 m. Also, for the scenarios using fixed bottom of resonator z_R, we observed for both cases a decrease in α factor (Figure 7c2). The two test scenarios show the same trend, and the low standard deviation in the difference of the fitted parameters between same tremor episode (different reference scenarios) confirms that the trend in changing moulin geometry is a physical signal.

We assess our findings of noncircular moulin cross section and changing moulin geometry with a graphical inspection. To this end, we separately plot moulin water level against tremor frequency for seismic tremor

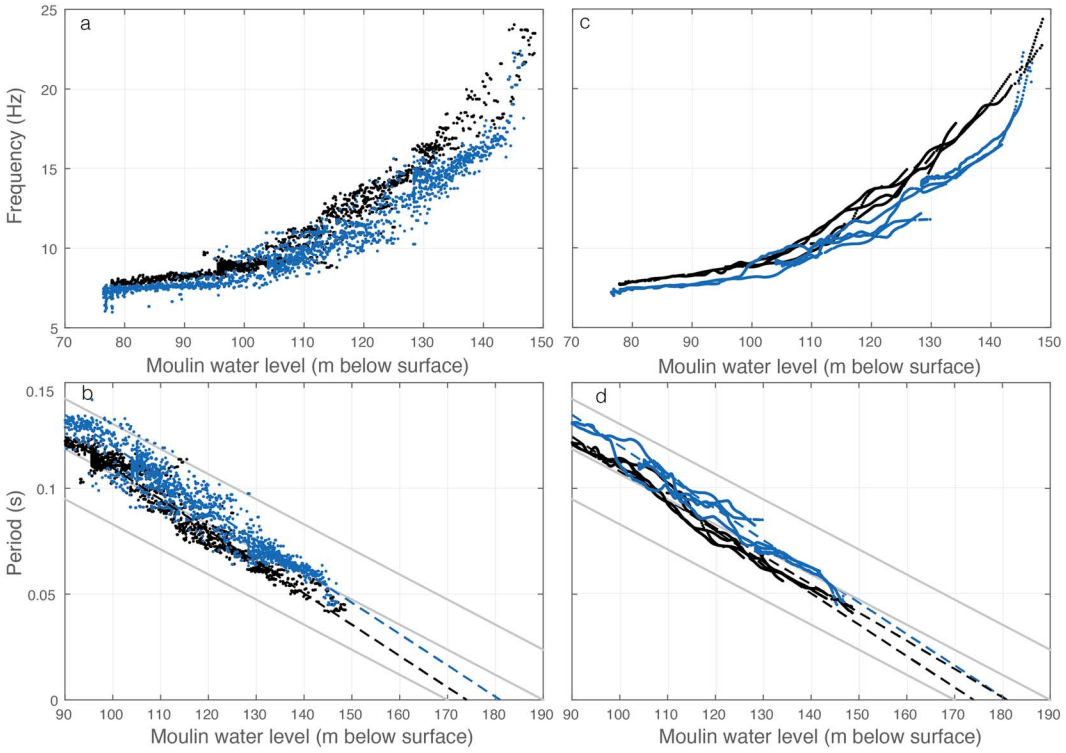

Figure 8. (a) Frequency and (b) period of the first overtone of the moulin tremor as a function of moulin water level during selected days early in the season (21 and 28 July 2011; black) and late in the season (11, 13, and 15 August; blue). In Figure 8b, the slope is inversely proportional to the tube wave speed and the intercept at period zero is the depth of the bottom of the resonator. The slope of the reference gray lines corresponds to a circular moulin cross section. An elliptical moulin gives a steeper slope. The dashed lines illustrate a possible scenario: a deepening of the resonator bottom throughout the season but no change in moulin ellipticity. (c and d) Same data as in Figures 8a and 8b but with smoothing (running average) applied to the frequency measurements. An additional dashed black line in Figure 8d illustrates a scenario in which the moulin ellipticity increases throughout the season, but the resonator bottom remains fixed.

recorded on 21 and 28 July and for 11, 13, and 15 August (Figure 8a) representing an earlier and later period during instrument deployment, respectively. In the absence of moulin geometry changes, equation (1) predicts that all points lie on a single curve. However, the two point clouds do not coincide and therefore confirms the idea of a changing moulin geometry. Figure 8b furthermore shows the same data but with the frequency axis replaced by its inverse (period). In this case, equation (1) predicts that the points lie on a straight line, whose slope is determined by the tube wave phase velocity c_R, which in turn depends on its cross-section ellipticity α. It also predicts that the straight line intercepts the coordinate axes at the resonator bottom depth z_R. The raw point clouds associated with the two time periods differ but seem almost parallel, which is consistent with a deepening moulin bottom. On the other hand, their overall slopes are different from what is expected for a circular cross section, confirming our previous finding. Figures 8c and 8d shows the same data after smoothing the logarithm of frequencies by a sliding average. Smoothing makes it apparent that another possible scenario is a change in resonator ellipticity but fixed resonator bottom depth, which illustrates our previous discussion on the trade-off between these two model parameters.

In conclusion, our hypothesis of steady geometry of the resonance body was rejected. The changing geometry may be caused by a combination of deepening resonator bottom (increasing z_R) and increasing cross-section ellipticity (decreasing α). Whereas we are not able to separate the influence of the two varying parameters, the overall physical resonance system clearly evolved during the 29 days of seismic observations.

4.3. Particle Motions and Wave Types

Classical approaches known from earthquake seismology are used to describe source mechanisms of seismic signals observed in glacial environments, for instance, with first motion polarity of *P* waves [e.g., *Zoet et al.*, 2012] or moment tensor inversions [e.g., *Walter et al.*, 2009]. Due to our continuous hour-long tremor signal,

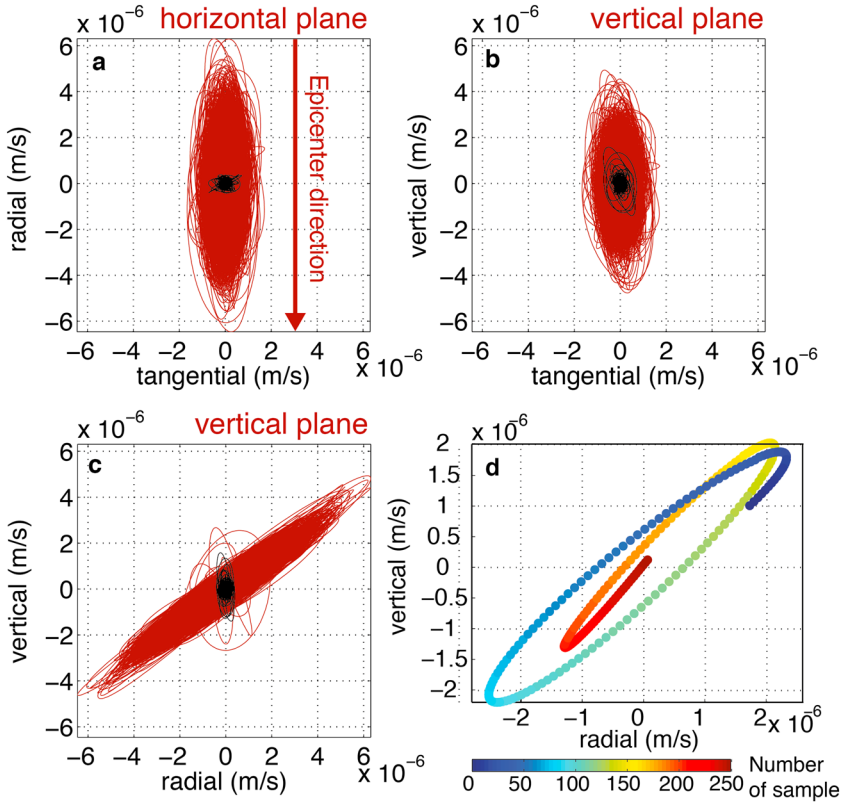

Figure 9. Particle motion for 20 min of observed waveform during tremor (red) and morning hours (background noise, black) with horizontal components oriented with the moulin location. (a) Radial and tangential components with elongation in radial direction. (b) Vertical and tangential components with elongation in vertical direction and low amplitude in tangential direction. (c) Radial and vertical component with elongation and inclination of about 45° indicating dependence on source depth. Figures 9a–9c are drawn with same scale for all axes. (d) Particle motions of vertical and radial component with colored points denoting the number of sample (with 500 Hz sampling frequency). We assume that the particle motion was built by the interference of continuously arriving *SV*, *P*, and Rayleigh waves with dominating *SV* and *P* waves.

different phases overlap and traditional source mechanism inversion techniques are not applicable. Hence, we investigated three-component particle motions to extract characteristics of the observed wave types and indications for source properties [*Aki and Richards*, 2002]. The seismometers were installed at different distances and in a circular configuration around the moulin (Figure 1). In order to compare the particle motion of waves emitted by the moulin source and measured by different seismic stations, we rotated the horizontal seismic waveforms (north and east) into radial and transverse direction. We concentrated our analysis and modeling on the orientation of the particle motion, extracted from relative amplitudes between different components, as the absolute measured amplitudes experienced unknown perturbations due to site effects and to the installation of the sensors on the glacier surface (including different coupling and leveling).

Figures 9a and 9c show the particle motions (red) observed at station FX07 located 377 m from the moulin during 20 min of tremor activity and during 20 min of background noise recorded at 6 A.M. the same day (black). The seismograms were Butterworth filtered (two-pole) from 3 to 5 Hz, including the fundamental mode of the moulin tremor at the time when the moulin water level was highest. The lower filter cutoff of 3 Hz additionally reduces the possible influence of dispersion on Rayleigh waves due to the sensitivity of longer wavelengths to the ice sheet bed [*Walter et al.*, 2015a].

The particle motions of the moulin tremor in Figures 9a–9c show high amplitudes in radial and vertical components and small amplitudes in tangential direction. Thus, the tremor consisted of mainly *P* waves, *SV* waves, and Rayleigh waves, with few or no *SH* waves and Love waves, consistent with a nearly axisymmetric moulin geometry. The observed particle motion (Figure 9d), a retrograde rotating ellipse, results from the convolution

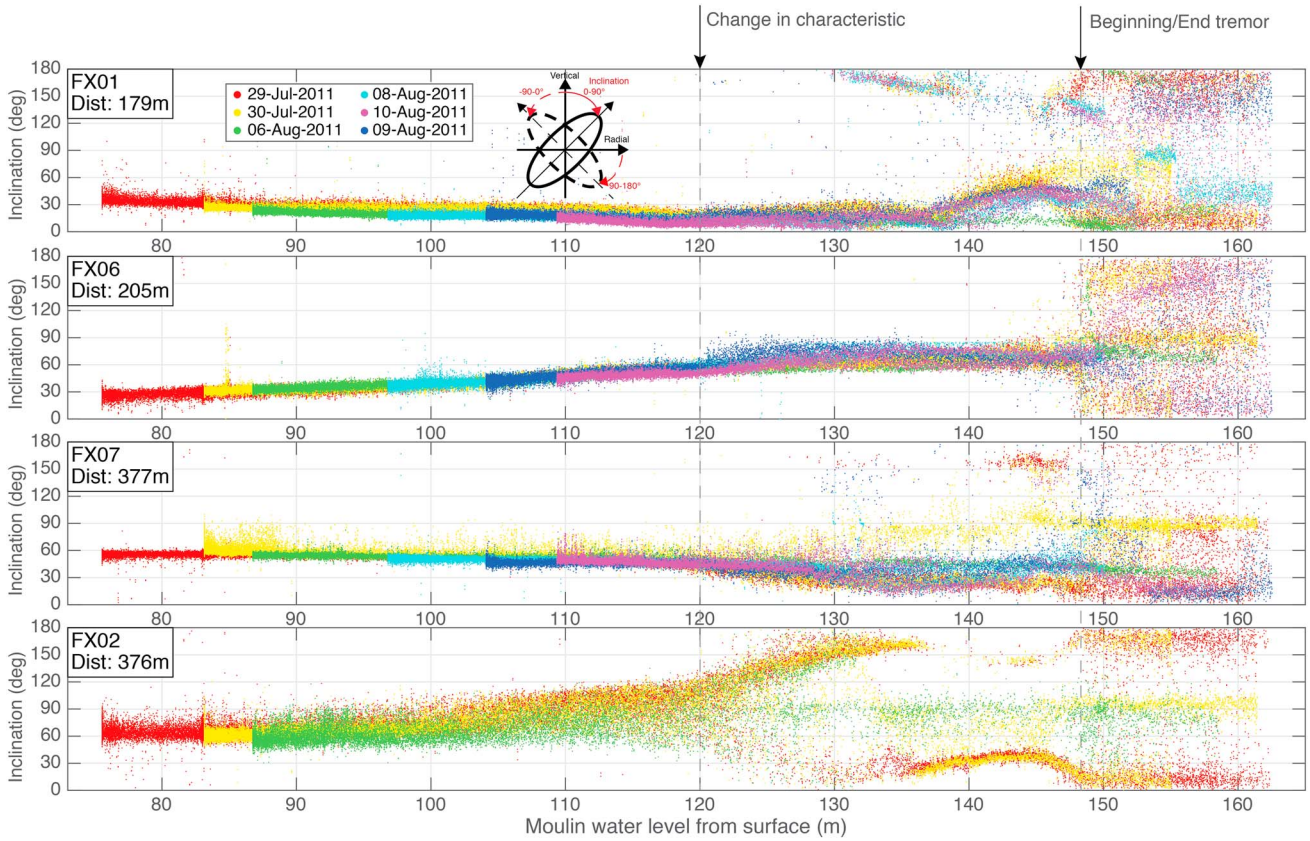

Figure 10. Comparison of inclination of particle motion (*y* axis) depending on the moulin water level (*x* axis) for the four stations FX01, FX06, FX07, and FX02 (from top). Positive inclination is defined as clockwise rotation from a vertical orientation (small inset). The inclination changes for all stations depending on time, however, is consistent for different days of observations and maximum water level of the tremor episode (colors). From about 120 m there is a change in behavior (higher scattering) and the tremor episode begins and ends with a water level of about 148 m (diffuse scattering). Both thresholds in water levels are marked with black arrows.

of an impulsive source seismogram and a sustained source time function. The source is excited continuously during several hours and radiates continuously *P* and *SV* waves, whose interference generates the observed wave field.

4.3.1. Ellipse Inclination: Dependence on Source-Receiver Geometry

The wave composition at various distances from the moulin is affected by the different amplitude-versus-distance decay of the waves generated by the two source mechanisms, the cylindrical source, and the bottom source [*Chouet*, 1985]. In addition, the bottom source is assumed to be a point source located at the bottom of the resonator, at a constant position during each tremor episode (constant bottom of resonator). In contrast, the cylindrical source is of finite extent. As a distribution of surface sources along the cylinder walls and thus its centroid depth, the cylindrical source induced particle motion depending on the moulin water level.

To analyze quantitatively the inclinations during one tremor episode, we estimated the orientation based on the orientation of eigenvectors determined by singular value decomposition [*Flinn*, 1965] for moving time windows of 5 s with 60% overlap. The data was filtered prior to the processing with a Butterworth (two-pole) band-pass filter to include the frequency bands of interest (Figure 2). The sliding window of 5 s includes several wave cycles (15 for 3 Hz) and allows for high temporal resolution. In the following, the ellipse inclination is defined by the angle between the vertical axis and the major axis of the ellipse, based on the radial (*x* axis) and vertical (*y* axis) components, with positive values (0–90°) in clockwise direction. Note the 180° symmetry of the ellipse orientation.

In Figure 10, inclinations (*y* axis) calculated during a tremor episode are compared with the moulin water level (*x* axis) for four particular stations (FX01, FX06, FX07, and FX02) installed at different distances and azimuths from the moulin. The data stream was filtered prior to the processing between 3 and 11 Hz with a Butterworth (two-pole) band-pass filter to also include the energy in higher-frequency bands during the first and

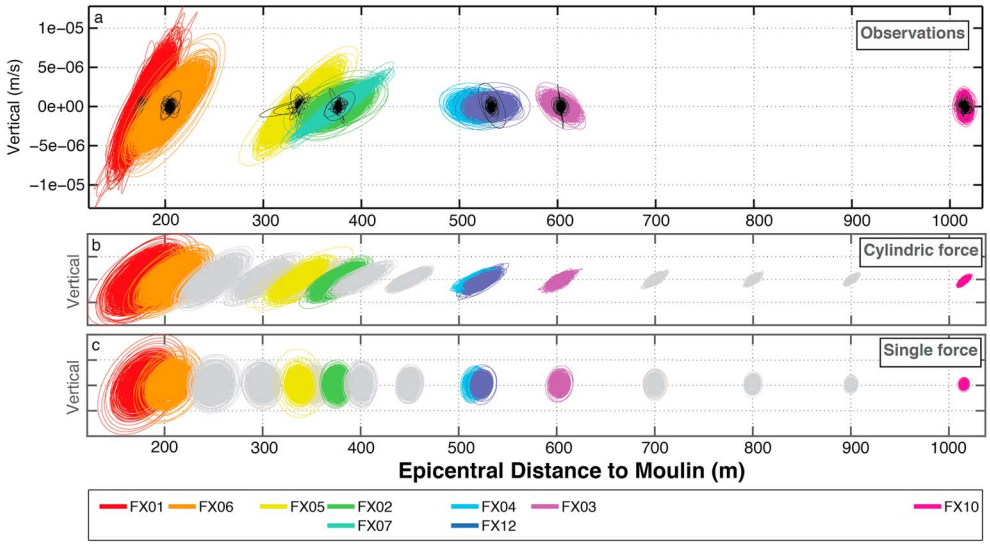

Figure 11. Particle motions of vertical and radial components Butterworth filtered between 3 and 5 Hz for different stations drawn in dependence on distance from the source. Scale for particle motions is identical for both axes. (a) Seismometer observations of particle motions, calculated for a time window of 2 h when moulin water level was highest (95.63 m below the surface). Colors correspond to measurements of seismometer installed in different distance from the source; black traces correspond to the noise level of a certain station in the morning. (b) Particle motion ellipses (grey and colored) modeled with a cylindrical source with 80 m in height. Amplitude is normalized. Colored ellipses highlight simulations at distances of stations shown in Figure 11a. (c) Particle motions modeled with a single force located in 175 m depth below the ice surface. Amplitude is normalized.

last part of one tremor episode (Figure 2). The stations were chosen due to their SNR and availability during the campaign. The time series for five different days (different colors), each with different peak water heights, are shown in Figure 10. For station FX02 only three tremor episodes are drawn due to low SNR. The inclination for each station changed continuously during a tremor episode and showed the same trend (slope is constant) for different tremor episodes (different colors) for water levels between 120 m and 75 m from the surface. For observations with concurrent water level between 120 m and about 148 m, the slope and scattering of the observed inclinations are different. For water level lower than 148 m, the moulin stopped emitting seismic tremors. Stations FX01 and FX07 measured decreasing inclination (rotation anticlockwise) with lower water level, whereas the inclinations at stations FX06 and FX02 showed the opposite dependence on water level. Stations FX07 and FX02 or FX01 and FX06, respectively, were installed at about the same distances from the source but with about 90° azimuthal difference (Figure 1). We therefore conclude that the height of the resonating water column and the seismometer location defined at first order the orientation of the tremor particle motion.

The moulin water level was a fast-changing system that might have influenced the seismic signal measured by the different stations through changes in distance from the source. We therefore focus first on a stable condition with maximum water level that was sustained during at least 1 h of tremor and compare the particle motion measured simultaneously by several stations located at different distances from the moulin. Figure 11a shows the observed particle motions for a 20 min window (two-pole Butterworth filtered, 3–5 Hz) in the radial-vertical plane, for different seismic stations (colors), as a function of the station distance from the source (x axis). Black traces represent the background noise in the morning of the same day. The inclination of the observed particle motion rotates clockwise with increasing distance, from around 30° for the closest station (FX01, Figure 11, red) up to nearly vertical at the farthest station (FX10, Figure 11, pink).

In order to better asses this tilting of the particle motion depending on distance from source, we simulated the formation of our signal by the interference of seismic waves emitted from a cylindric and bottom seismic source as explained in detail in the following paragraph. The cylindric source mainly lead to a clockwise tilted ellipse (Figure 11b), whereas the bottom source generates waves with mainly vertical particle motion (Figure 11c). Our modeling aimed at estimating the ratio between cylindric and bottom sources.

4.3.2. Waveform Modeling Combining Cylindric and Bottom Sources

We used the frequency-wave number method of *Zhu and Rivera* [2002] to calculate theoretical Green's functions, assuming a half-space consisting of an ice layer of 623 m thickness underlaid by granite bedrock [*Walter et al.*, 2015a]. We used *P* and *S* wave velocities in ice of 1.95 km s^{-1} and 3.87 km s^{-1}, respectively [*Walter et al.*, 2015a], and an attenuation quality factor *Q* of 5 and 10 for *S* and *P* waves, respectively [*Röösli et al.*, 2014]. The granitic basement was modeled with velocities and attenuation quality factor for *P* waves of 6.2 km s^{-1} and 400, and for *S* waves 3.6 km s^{-1} and 200, respectively [*Walter et al.*, 2015a]. Due to the shallow depth of the borehole sensors (2–3 m) relative to the wavelengths of interest, we neglect their depth in our analysis. The method of *Zhu and Rivera* [2002] for wave modeling can reproduce both dynamic and static displacement components, including near-field terms. We assumed a point force at the bottom of the resonator (disk enclosing the resonance body, Figure 5) in combination with a symmetric cylinder force, consistent with negligible observed *SH* phases (Figure 9). The bottom source was defined by dip and strike angles of 90° (vertical force pointing downward). The cylinder source was represented by a diagonal moment tensor with $M_{11} = M_{22} = \lambda + \mu$ and $M_{33} = \lambda$ [*Chouet*, 1985], where $\lambda = 6.79$ GPa is the first Lamé constant of ice. The cylinder source was generated as a weighted superposition of elementary cylinder sources located at different depths with a step size of 5 m. The weights reflect the pressure versus depth distribution of the fundamental mode of the semiopen resonator: $p(z) \propto \cos(\pi/2(z - z_R)/(H_R - z_R))$.

In a second step, we convolved the simulated Green's functions (bottom and cylinder sources) with white noise to generate a continuously radiating seismic signal. Note that the source time function of the bottom and cylinder sources is the same.

To estimate the ratio between the simulated cylindric and bottom sources, we used observations of three different tremor episodes with same maximum water height of 95 m below surface (Figure 12a, 31 July, 5 August, and 6 August 2011). We estimated the orientation of the ground motion ellipse over a 50 min long window of seismic tremor with quite constant moulin water level (±1 m) such that the orientation is expected to be stable. The tremor waveform was Butterworth filtered (two-pole) between 3 and 5 Hz including the tremor's fundamental mode. We processed the data with 5 min sliding windows and 60% overlap, calculating azimuth and inclination by linear robust least squares fit. We excluded stations with a measured ground motion azimuth departing by more than 30° from the station-moulin azimuth. Other stations were reoriented to the station-moulin azimuth because we expect uncertainties in the manual orientation of the seismometers. After the orientation, we repeated the procedure of calculating the inclination and best fit value. The error bars shown in Figure 12a (with zoom a1 and a2) correspond to the range of calculated inclination angles including 95% of the values. The increasing error bars for larger distance are mainly caused by a low SNR.

The best fit between observed (Figure 12a) and simulated (Figure 12b) ground motion inclinations was derived with 0.45 weight on the bottom source (Figure 12b3). We excluded FX10 (1015 m distance from the source) in our fitting procedure as the SNR was low and the uncertainty was high (see error bars in Figure 12a). Figure 12b shows the comparison of the observed data (grey) and the best fit model (orange) with bottom source (purple) and cylindric (blue) sources as references. Data points were calculated at distances of installed seismometers, at every 50 m between 200 and 600 m, and at every 100 m between 600 and 1000 m. The zoom in Figure 12b1 shows the modeled (colors) and observed (grey points) data at the stations FX05 and FX09 for all three tremor episodes and additionally FX02 on 31 July 2011 and FX07 on 6 August 2011. The zoom in Figure12b2 shows stations FX04, FX12, FX08, and FX03 (increasing distance). The weight of 0.45 corresponds to a ratio of ~250 m between the seismic moment of the cylindric source and the force of the bottom source. This ratio can be shown to be proportional to the height of the resonator, *D*. For the first resonance mode the ratio is predicted to be $3\sqrt{(2)}D/\pi \sim 1.35D$, if the bottom and the bulk of the resonator have the same cross-section area. The resulting estimate $D \sim 185$ m is higher but of the same order of magnitude as the resonator height we inferred previously from the relation between tremor frequency and moulin water level. Given the approximations in our analysis, this order-of-magnitude agreement is notable.

The modeled seismic source follows the observed changes in inclination with a root mean square value (RMS) lower than 3°. Nevertheless, the limitations of our method are apparent: the observed inclination at FX08 is around 20° different than at FX04 and FX12, which are located only 20 and 10 m closer to the source, respectively (Figures 12a2 and 12b2). This discrepancy could be explained by a nonaxisymmetric source or by different path and site effects at these stations.

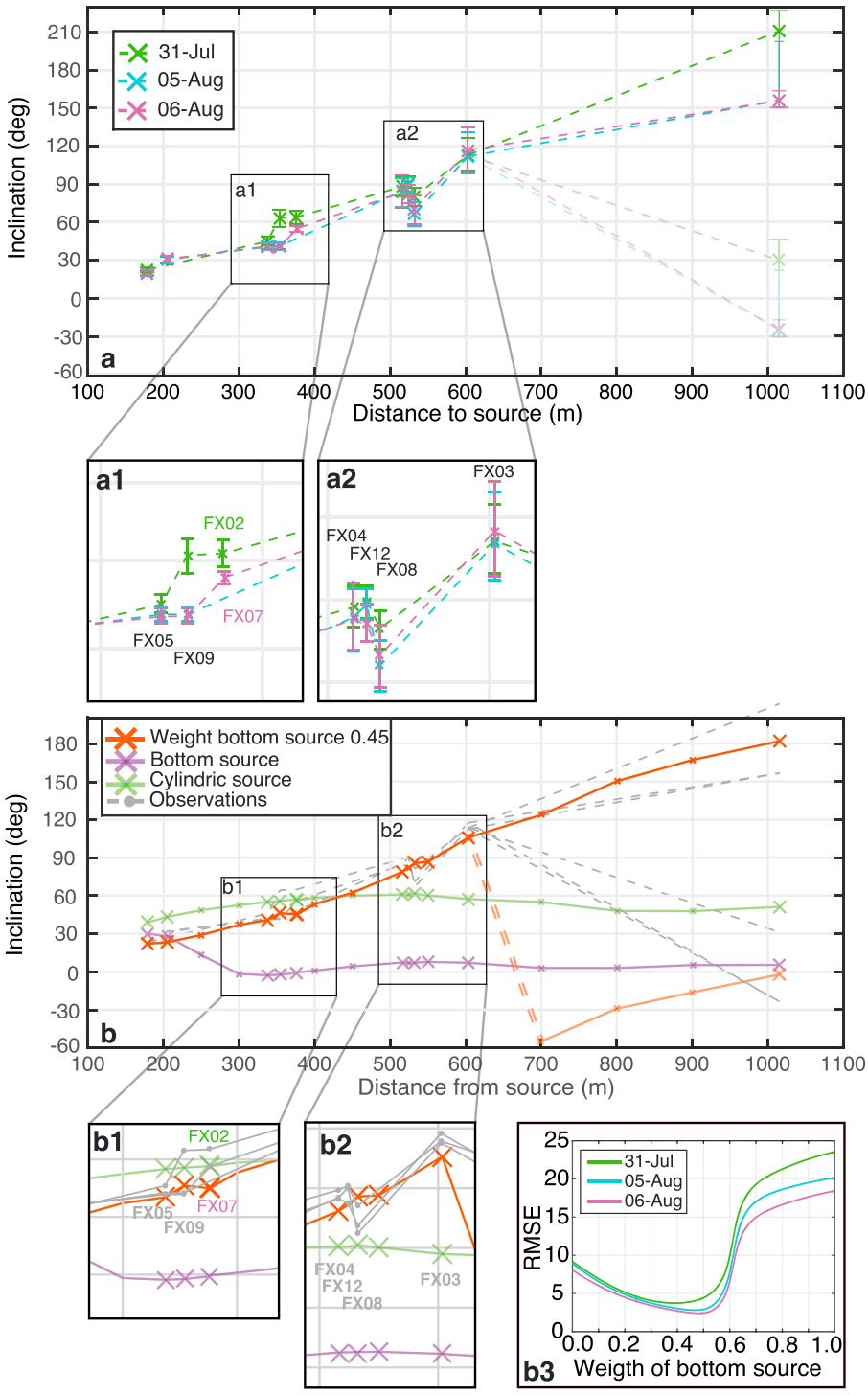

Figure 12. Measured inclination and corresponding simulations of three tremor episodes observed with the entire seismometer network. (a) Observation (colored crosses) of three tremor episodes for a time window with same (maximum) water level inside the moulin of 95 m below the surface. (a1 and a2) The zoom in 200–400 m and 450–650 m distance to source, respectively. (b) Observations (grey) and corresponding simulations (colored) for the tremor source. Large crosses denote distances with seismic observations. The orange curve shows the best fit simulation with 0.45 weight on the bottom source (in 175 m depth) and 0.55 weight on the cylindric source (located in 95–175 m below surface). (b1 and b2) The zoom in 200–400 m and 450–650 m distance to source, respectively. (b3) Best fit curve with best weight of 0.45 for bottom source (lowest RMS). Different colors mark the days of observations. Note the 180° symmetry of the ellipse orientation, especially important for station FX10 (1015 m from the moulin), represented in Figures12a and 12b with an additional transparent line connected to the solution for station FX10.

5. Discussion

5.1. First-Order Mechanism

With our seismic observations, we were able to adapt a source model developed in volcano tremor seismology to the glacial environment (Figure 5) and thus to monitor the interior of a moulin. The seismic moulin tremor was excited by the surface stream falling onto the water surface and was resonating in the cylindrical water column. The tremor was excited when the water reached a certain height and its amplitude was controlled by the amount of inflowing water. The frequency content and particle motion of the emitted seismic waves evolved from the interaction of the resonating cylindric water column with the solid walls and the bottom of the resonator.

In our model, the surface stream ended in a water fall of several tens of meters in height before hitting the water surface inside the moulin. We showed that a section of the water-filled moulin then resonated following the one-side closed organ pipe model [*Chouet*, 1985], whereby we observed up to three modes of resonance. With the inversion for z_R (equation (1)) representing the bottom of the resonator, we constrained the (changing) height of the resonator to 20–75 m. We propose that a kink about 180 m below the ice surface (30% of the ice sheet thickness) enclosed the resonating body at the bottom (Figure 5). Furthermore, a cross-section ellipticity ratio α between 0.3 and 0.5 suggests an elliptical shape of the vertical conduit. Complex moulin conduit geometries, different from a purely vertical shaft, have been reported by, e.g., *Reynauld* [1986] and *Catania et al.* [2008]. This resonance body changed over the course of the season toward a more complex geometry and/or larger depth, respectively. Expected changes inside the moulin are caused by frictional heating from the interaction between flowing water and ice, viscous creep of ice closing englacial channels, and the ice sheet flow [*Cuffey and Paterson*, 2010]. However, due to fast-changing input of meltwater into the conduit, the processes are seldom in balance [e.g., *Nye*, 1969; *Gulley et al.*, 2009; *Andrews et al.*, 2014], which is confirmed by our analysis.

We also demonstrated that two different types of sources, a cylindric and a bottom source, were required to model our moulin tremor [*Chouet*, 1985]. Our analysis confirmed the dominance of the cylindric source in the near field and the dominance of the bottom force in the far field (Figure 11). The modeling results shown in Figure 12 were achieved with a static configuration with a same and constant moulin water level for three different tremor episodes and thus stable particle motion over a time window of at least 1 h. We estimated the ratio between the two source types (both normalized amplitudes) as 0.45. This value different than zero or one is the expression that we require a combination of both sources in order to model the near field and far field.

Our observations originated in the context of a highly dynamic system with the ice continuously deforming and with large fluctuation in meltwater input into the moulin. As already seen in Figure 10, the measured inclination changes with the moulin water level depend on distance from the source, azimuth, and absolute water level. For instance, stations FX02 and FX07 were located at the same distance from the moulin with a difference in azimuth from the source of about 90° (Figure 1). The dependence of inclination on water level is opposite for the two stations with decreasing inclination for lower water level (rising distance to surface) for FX02 and synchronous increase for FX07. In the contrary, different tremor episodes showed the same temporal change in particle motion for a certain station, implying a relatively stable geometry of the source to first order.

In order to assess the (nonlinear) influence of the moulin's changing water level, the particle motion simulations (Figure 12) were extended to include variations in water level. Figure 13 shows the days 29 July and 6 August 2011, also shown in Figure 10, for four particular seismic stations. In addition, the red and green lines correspond to the modeled inclination accounting for a possible deepening of the bottom of the resonator during the season (Figure 7). Nevertheless, the effect of a change of bottom of resonator of 5 m is small and affects only waveforms of the closest station FX01, also indicated by the observations on 6 August (green) of lower inclinations than for observations on 29 July 2011 (red). In general, we observed a decreasing inclination angle with decreasing water level for all simulated distances in agreement in trend, but smaller in slope, with our observations at stations FX01 and FX07 located east and ESE from the moulin (Figure 1). FX02 and FX06 were located upstream and downstream from the moulin, respectively, and showed an opposite trend in inclination variation.

The reasons for the discrepancy between the simulations and the observations can be diverse in origin. Our modeling included the assumption of two horizontal layers of constant attenuation and velocity and a constant ratio between the two source types with symmetric radiation pattern. However, the estimated ratio

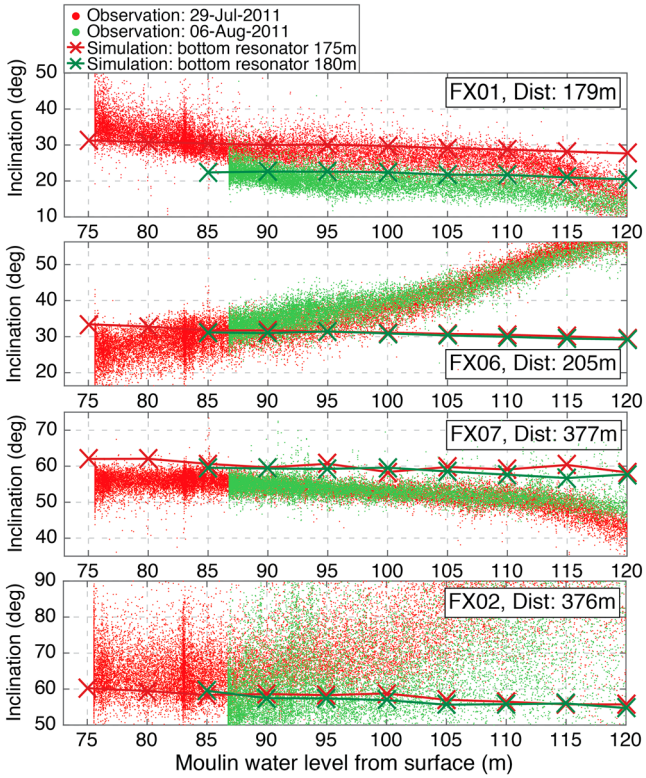

Figure 13. Observed inclination of particle motion (*y* axis) with the simultaneously observed water level inside the moulin (*x* axis) is shown for two tremor episodes (red and green dots) observed on four stations (same observations as in Figure 10). Green and red lines correspond to simulated waveforms with the model of a bottom source (disk at moulin bottom) and cylindric source (height of resonating water column). The green and red curves consider the change in depths of the bottom of the resonator. A lower resonator bottom mainly affects the closest station FX01 (lower inclination). Possible reasons for the divergence between the simulations and the observations are discussed in the manuscript text.

between the two source types might also change depending on water level. Furthermore, the glacier bed topography at our study site was highly complex [*Ryser et al.*, 2014b], which might have influenced the seismic signal depending on azimuth due to refraction and reflection on the glacier bed. However, using a 3-D glacier bed topography with a 3-D velocity model would include many additional model parameters. Our estimation of the conduit cross-section ellipticity α and the particle motion shown in Figure 11 points in addition toward an asymmetric radiation pattern. The particle motion observed at station FX07 (Figure 11 turquoise) is more elongated than that at FX02 (Figure 11 green) installed at the same distance.

These possible reasons might explain the mismatch between the observations and the modeling of the time dependent and dynamic system within a tremor episode. For a more detailed analysis, we are, nevertheless, mainly limited by the observational geometry as only station FX10 was installed far enough from the source that the bottom source dominated the particle motion (purple, almost vertical ellipse in Figure 11). Due to the distance of 1015 m, the signal observed at FX10 was too weak for a more detailed analysis. In addition, the seismic observations on an ice sheet involve other difficulties influencing the result and interpretation: background noise is high due to continuous meltwater flow [*Walter et al.*, 2008; *Röösli et al.*, 2014], a stable and leveled seismometer installation is difficult to achieve (mainly influencing amplitude), wave velocities are less well known, and attenuation factor depends on depth-dependent ice temperature [*Peters et al.*, 2012; *Ryser et al.*, 2014a].

5.2. Further Tremor Characteristic

The presented seismic source model accounts for large-scale and main physical processes that lead to the observed seismic tremor. In addition, we observed several second-order effects that modified the first-order tremor characteristics.

The most striking second-order characteristics visible in the spectrograms of Figure 2 are the two different types of low-energy band gaps (labels A and B). Horizontal band gaps were observed for the entire observation period and with the entire network with the same absorbed frequencies (see Text S1). We suggest that waves were trapped in fractures along the moulin walls absorbing certain frequency bands, that possible water cavities below the bottom of the resonator (>180 m) were absorbing energy and acted as another resonator body, or that we observed the effect of bubble resonance inside the moulin shaft [e.g., *Ichihara et al.*, 2004; *Mani et al.*, 2010]. The existence of englacial fractures inside a borehole has already been reported by *Fountain et al.* [2005] and *Walter et al.* [2009], and fractures are also a common feature for moulin walls (K. Steffen, personal communication, 2015).

In the spectrograms shown in Figures 2d and 7b, the beginning of the moulin tremor is accompanied by some seismic energy below 5 Hz with an earlier onset than the higher frequencies. Especially, the energy emitted in the second resonance mode is delayed relative to the beginning in lower frequencies (Figure 7b, grey points in Figure 7a). We defined the beginning of the tremor signal as soon as we observed enhanced coherent energy between 3 and 5 Hz most probably when the water fall hit the water surface. Thus, the resonating body needs some time until the resonance is fully developed and higher modes are observable. An indication for a complex volumetric geometry at the base of the resonator supporting these findings is shown in Figure 13 with a change in the time series of ellipse orientation with moulin water level of 120 m and lower. Thus, this water level corresponds to the beginning and end of the tremor episode, when higher-frequency contents were absorbed visible with the horizontal band gaps in the spectrograms (Figure 2, label A).

In addition, we observed enhanced energy (yellow) before the beginning of the tremor (red colors), mainly visible in Figure 2d. Even for days where the (resonating) moulin tremor was inactive, we recorded enhanced energy in the frequency bands typical for the moulin tremor (see Figure S1). We therefore suggest that in the water fall hitting the ice generated background noise; however, no amplification with the water body is possible in this case. These interpretations are also supported by ambient noise analysis by *Walter et al.* [2015b], who processed the same data set and observed a continuous seismic source from the moulin with distinct frequency peaks of 4 and 6 Hz, even when the moulin tremor was inactive.

Nevertheless, the question remains as to why this particular moulin generates such a seimic tremor and how dependent the seismic emissions are on a particular geometry inside the moulin. The second moulin located within our network did not generate a measurable moulin tremor [*Röösli et al.*, 2014]. It can be expected that the water fall of the englacial stream entering this particular moulin, though one magnitude smaller in discharge, also generated noise by hitting ice or the water surface. Due to the dominance of our primary moulin tremor, we are not able to see this small signal from another moulin, if existent.

6. Conclusion

For the first time, we were able to monitor and constrain moulin geometry and water flow processes with seismic waveforms. The tremor waveform was generated by the surface stream triggering acoustic waves resonating in the cylindric moulin shaft and consisting of two types of wave sources: A vertical point force at the bottom of the resonator and a distribution of surface forces resulting from the interaction of the water-filled pipe with the solid ice walls. We thus directly observed waveforms generated with characteristics of the model for volcanic tremors proposed by *Chouet* [1985] in a nonvolcanic regime and transposed it to glaciers, as an example of a fast-changing, dynamic system. The dominance of such a tremor inside our dense seismometer network opened the unique possibility to study a seismic tremor and its evolution over several weeks and connect long-term evolution (during the season) with short-term changes (during one tremor episode).

The first-order effects with the trigger and the following resonance characterized the large-scale seismic system. The seismic signal, nevertheless, contains still different information with second-order effects that additionally constrain englacial conditions. As passive seismic observations are noninvasive and connected with low installation costs, they are a powerful technique to investigate and monitor subglacial drainage systems including moulins, and changes thereof.

Acknowledgments
This project was funded by Swiss Federal Institute of Technology Zürich (ETH) under grant ETH-27 10-3. The salary of F.W. was partially funded by the European Union Seventh Framework Programme (FP7-PEOPLE-2011-IEF) under grant agreement 29919 and by the Swiss National Science Foundation (GlaHMSeis Project PP00P2_157551). This work was partially supported by grants from the Swiss National Science Foundation (200021_127197 SNE-ETH (ROGUE)) and the Arctic Natural Sciences Program of the US National Science Foundation (OPP-0909454 and OPP-0908156). Waveform processing and plots were done with MathWorks MATLAB and Obspy (A Python Toolbox for seismology/seismological observatories). We thank Brad Lipovsky, Naofumi Aso, and one anonymous reviewer for their review that helped to improve the quality of the paper. We are grateful to many members of the Institute of Geophysics, the Swiss Seismological Service and the Laboratory of Hydraulics, Hydrology and Glaciology of ETH Zürich. S. Husen provided valuable support for preparation and conduction of the seismological monitoring. Importantly, M. Lüthi initiated the ROGUE project opening access to logistical and scientific support for the present study. We thank M. Funk, V. Tsai, F. Gimbert, P. Dalban Canassy, and L. Andrews for interesting discussions. We also thank T. Wyder, C. Senn, K. Plenkers, S. Hiemer, M. Meier, C. Birchler, A. Bauder, R. Hawley and B. Morriss, M. J. Hoffman, and G. Catannia for their help during the field campaign in Greenland and making it all possible. Seismic waveform data are available via arclink.ethz.ch using network code XH.

References

Aki, K., and P. G. Richards (2002), *Quantitative Seismology*, 2nd ed., Univ. Sci. Books, Sausalito, Calif.

Aki, K., M. Fehler, and S. Das (1977), Source mechanism of volcanic tremor: Fluid-driven crack models and their application to the 1963 kilauea eruption, *J. Volcanol. Geotherm. Res.*, *2*(3), 259–287, doi:10.1016/0377-0273(77)90003-8.

Andrews, L. C., G. A. Catania, M. J. Hoffman, J. D. Gulley, M. P. Lüthi, C. Ryser, R. L. Hawley, and T. A. Neumann (2014), Direct observations of evolving subglacial drainage beneath the Greenland Ice Sheet, *Nature*, *514*(7520), 80–83, doi:10.1038/nature13796.

Bartholomaus, T. C., J. M. Amundson, J. I. Walter, S. O'Neel, M. E. West, and C. F. Larsen (2015), Subglacial discharge at tidewater glaciers revealed by seismic tremor, *Geophys. Res. Lett.*, *42*, 6391–6398, doi:10.1002/2015GL064590.

Bartholomew, I., P. Nienow, D. Mair, A. Hubbard, M. A. King, and A. Sole (2010), Seasonal evolution of subglacial drainage and acceleration in a Greenland outlet glacier, *Nat. Geosci.*, *3*(6), 408–411, doi:10.1038/ngeo863.

Bartholomew, I., P. Nienow, A. Sole, D. Mair, T. Cowton, and M. A. King (2012), Short-term variability in Greenland Ice Sheet motion forced by time-varying meltwater drainage: Implications for the relationship between subglacial drainage system behavior and ice velocity, *J. Geophy. Res.*, *117*, F03002, doi:10.1029/2011JF002220.

Bell, R. E. (2008), The role of subglacial water in ice-sheet mass balance, *Nat. Geosci.*, *1*(5), 297–304, doi:10.1038/ngeo186.

Benn, D., J. Gulley, A. Luckman, A. Adamek, and P. Glowacki (2009), Englacial drainage systems formed by hydrologically driven crevasse propagation, *J. Glaciol.*, *55*, 513–523, doi:10.3189/002214309788816669.

Biot, M. A. (1956), Theory of propagation of elastic waves in a fluid-saturated porous solid. I. Low-frequency range, *J. Acoust. Soc. Am.*, *28*(2), 168–178.

Box, J. E., and W. Colgan (2013), Greenland ice sheet mass balance reconstruction. Part III: Marine ice loss and total mass balance (1840–2010), *J. Clim.*, *26*(18), 6990–7002, doi:10.1175/JCLI-D-12-00546.1.

Carmichael, J. D., I. Joughin, M. D. Behn, S. Das, M. A. King, L. Stevens, and D. Lizarralde (2015), Seismicity on the western Greenland Ice Sheet: Surface fracture in the vicinity of active moulins, *J. Geophys. Res. Earth Surf.*, *120*, 1082–1106, doi:10.1002/2014JF003398.

Catania, G. A., and T. A. Neumann (2010), Persistent englacial drainage features in the Greenland Ice Sheet, *Geophys. Res. Lett.*, *37*, L02501, doi:10.1029/2009GL041108.

Catania, G. A., T. A. Neumann, and S. F. Price (2008), Characterizing englacial drainage in the ablation zone of the Greenland ice sheet, *J. Glaciol.*, *54*(187), 567–578, doi:10.3189/002214308786570854.

Chandler, D. M., et al. (2013), Evolution of the subglacial drainage system beneath the Greenland Ice Sheet revealed by tracers, *Nat. Geosci.*, *6*(3), 195–198, doi:10.1038/ngeo1737.

Chouet, B. (1985), Excitation of a buried magmatic pipe: A seismic source model for volcanic tremor, *J. Geophys. Res.*, *90*(B2), 1881–1893, doi:10.1029/JB090iB02p01881.

Chouet, B. A. (1996), Long-period volcano seismicity: Its source and use in eruption forecasting, *Nature*, *380*(6572), 309–316, doi:10.1038/380309a0.

Chouet, B. A., and R. S. Matoza (2013), A multi-decadal view of seismic methods for detecting precursors of magma movement and eruption, *J. Volcanol. Geotherm. Res.*, *252*, 108–175.

Cuffey, K. M., and W. Paterson (2010), *The Physics of Glaciers*, 4th ed., Academic Press, New York.

Das, S. B., I. Joughin, M. D. Behn, I. M. Howat, M. A. King, D. Lizarralde, and M. P. Bhatia (2008), Fracture propagation to the base of the Greenland Ice Sheet during supraglacial lake drainage, *Science*, *320*(5877), 778–781, doi:10.1126/science.1153360.

Dunham, E. M., and D. E. Ogden (2012), Guided waves along fluid-filled cracks in elastic solids and instability at high flow rates, *J. Appl. Mech.*, *79*(3), 031020.

Flinn, E. A. (1965), Signal analysis using rectilinearity and direction of particle motion, *Proc. IEEE*, *53*(12), 1874–1876, doi:10.1109/PROC.1965.4462.

Fountain, A. G., R. W. Jacobel, R. Schlichting, and P. Jansson (2005), Fractures as the main pathways of water flow in temperate glaciers, *Nature*, *433*(7026), 618–621, doi:10.1038/nature03296.

Gulley, J. D., D. I. Benn, E. Screaton, and J. Martin (2009), Mechanisms of englacial conduit formation and their implications for subglacial recharge, *Quat. Sci. Rev.*, *28*(19–20), 1984–1999, doi:10.1016/j.quascirev.2009.04.002.

Gulley, J. D., M. Grabiec, J. B. Martin, J. Jania, G. Catania, and P. Glowacki (2012), The effect of discrete recharge by moulins and heterogeneity in flow-path efficiency at glacier beds on subglacial hydrology, *J. Glaciol.*, *58*(211), 926–940, doi:10.3189/2012JoG11J189.

Harper, J. T., J. H. Bradford, N. F. Humphrey, and T. W. Meierbachtol (2010), Vertical extension of the subglacial drainage system into basal crevasses, *Nature*, *467*(7315), 579–582, doi:10.1038/nature09398.

Heeszel, D. S., F. Walter, and D. L. Kilb (2014), Humming glaciers, *Geology*, *42*(12), 1099–1102.

Helmstetter, A., L. Moreau, B. Nicolas, P. Comon, and M. Gay (2015), Intermediate-depth icequakes and harmonic tremor in an Alpine glacier (glacier d'Argentière, France): Evidence for hydraulic fracturing?, *J. Geophys. Res. Earth Surf.*, *120*, 402–416, doi:10.1002/2014JF003289.

Holmlund, P. (1988), Internal geometry and evolution of moulins, *J. Glaciol.*, *34*, 242–248.

Ichihara, M., H. Ohkunitani, Y. Ida, and M. Kameda (2004), Dynamics of bubble oscillation and wave propagation in viscoelastic liquids, *J. Volcanol. Geotherm. Res.*, *129*(1), 37–60.

Iken, A. (1981), The effect of the subglacial water pressure on the sliding velocity of a glacier in an idealized numerical model, *J. Glaciol.*, *27*(97), 407–421.

Iken, A., and R. A. Bindschadler (1986), Combined measurements of subglacial water pressure and surface velocity of Findelengletscher, Switzerland: Conclusions about drainage system and sliding mechanism, *J. Glaciol.*, *32*(110), 101–119.

Lawrence, W., and A. Qamar (1979), Hydraulic transients: A seismic source in volcanoes and glaciers, *Science*, *203*(4381), 654–656.

Lay, T., and T. C. Wallace (1995), *Modern Global Seismology*, vol. *58*, Academic Press, San Diego, Calif.

Lesage, P., F. Glangeaud, and J. Mars (2002), Applications of autoregressive models and time–frequency analysis to the study of volcanic tremor and long-period events, *J. Volcanol. Geotherm. Res.*, *114*(3), 391–417, doi:10.1016/s0377-0273(01)00298-0.

Lipovsky, B. P., and E. M. Dunham (2015), Vibrational modes of hydraulic fractures: Inference of fracture geometry from resonant frequencies and attenuation, *Geophys. Res. Solid Earth*, *120*, 1080–1107, doi:10.1002/2014JB011286.

Lomax, A., J. Virieux, P. Volant, and C. Berge-Thierry (2000), Probabilistic earthquake location in 3D and layered models, *Mod. Approaches Geophys.*, *18*, 101–134, doi:10.1007/978-94-015-9536-0_5.

Mani, M., S. Mandre, and M. P. Brenner (2010), Events before droplet splashing on a solid surface, *J. Fluid Mech.*, *647*, 163–185.

Métaxian, J.-P., S. Araujo, M. Mora, and P. Lesage (2003), Seismicity related to the glacier of Cotopaxi Volcano, Ecuador, *Geophys. Res. Lett.*, *30*(9), 1483, doi:10.1029/2002GL016773.

Minakami, T. (1974), Seismology of volcanoes in Japan, in *Physical Volcanology*, edited by L. Civetta et al., pp. 1–27, Elsevier, Amsterdam, doi:10.1016/b978-0-444-41141-9.50007-3.

Norris, A. (1990), The speed of a tube wave, *J. Acoust. Soc. Am.*, *87*(1), 414–417.

Nye, J. F. (1969), A calculation on the sliding of ice over a wavy surface using a Newtonian viscous approximation, *Proc. R. So. A*, *311*(1506), 445–467, doi:10.1098/rspa.1969.0127.

Peters, L. E., S. Anandakrishnan, R. B. Alley, and D. E. Voigt (2012), Seismic attenuation in glacial ice: A proxy for englacial temperature, *J. Geophys. Res.*, *117*, F0200, doi:10.1029/2011JF002201.

Petrenko, V. F., and R. W. Whitworth (1999), *Physics of Ice*, Oxford Univ. Press, Oxford, U. K.
Reynauld, L. (1986), Correspondence. The November 1986 survey of the Grand Moulin on the Mer de Glace, Mont Blanc Massif, France, *J. Glaciol.*, *33*, 130–131.
Rignot, E., I. Velicogna, and M. R. van den Broeke (2011), Acceleration of the contribution of the Greenland and Antarctic ice sheets to sea level rise, *Geophys. Res. Lett.*, *38*, L05503, doi:10.1029/2011GL046583.
Röösli, C., F. Walter, S. Husen, L. C. Andrews, P. Martin, G. A. Catania, and E. Kissling (2014), Sustained seismic tremors and icequakes detected in the ablation zone of the Greenland ice sheet, *J. Glaciol.*, *60*(221), 563–575, doi:10.3189/2014jog13j210.
Ryser, C., M. P. Lüthi, L. C. Andrews, G. A. Catania, M. Funk, R. Hawley, M. Hoffman, and T. A. Neumann (2014a), Caterpillar-like ice motion in the ablation zone of the Greenland ice sheet, *J. Geophys. Res. Earth Surf.*, *119*, 2258–2271, doi:10.1002/2013JF003067.
Ryser, C., M. P. Lüthi, L. C. Andrews, M. J. Hoffman, G. A. Catania, R. L. Hawley, T. A. Neumann, and S. S. Kristensen (2014b), Sustained high basal motion of the Greenland ice sheet revealed by borehole deformation, *J. Glaciol.*, *60*(222), 647–660, doi:10.3189/2014JoG13J196.
Schroeder, J. (1998), Hans glacier moulins observed from 1988 to 1992, Svalbard, *Nor. Geogr. Tidsskr. - Norw. J. Geogr.*, *52*(2), 79–88, doi:10.1080/00291959808552387.
Sundal, A. V., A. Shepherd, P. Nienow, E. Hanna, and S. Palmer (2011), Melt-induced speed-up of Greenland ice sheet offset by efficient subglacial drainage, *Nature*, *469*(7331), 521–524, doi:10.1038/nature09740.
van der Veen, C. J. (2007), Fracture propagation as means of rapidly transferring surface meltwater to the base of glaciers, *Geophys. Res. Lett.*, *34*, L01501, doi:10.1029/2006GL028385.
Vatne, G. (2001), Geometry of englacial water conduits, Austre Brøggerbreen, Svalbard, *Nor. Geogr. Tidsskr. - Norw. J. Geogr.*, *55*(2), 85–93, doi:10.1080/713786833.
Walter, F., N. Deichmann, and M. Funk (2008), Basal icequakes during changing subglacial water pressures beneath Gornergletscher, Switzerland, *J. Glaciol.*, *54*(186), 511–521, doi:10.3189/002214308785837110.
Walter, F., J. F. Clinton, N. Deichmann, D. S. Dreger, S. E. Minson, and M. Funk (2009), Moment tensor inversions of icequakes on Gornergletscher, Switzerland, *Bull. Seismol. Soc. Am.*, *99*(2A), 852–870, doi:10.1785/0120080110.
Walter, F., P. Roux, C. Roeoesli, A. Lecointre, D. Kilb, and P. F. Roux (2015a), Using glacier seismicity for phase velocity measurements and Green's function retrieval, *Geophys. J. Int.*, *201*(3), 1722–1737, doi:10.1093/gji/ggv069.
Walter, J. I., I. Svetlizky, J. Fineberg, E. E. Brodsky, S. Tulaczyk, C. G. Barcheck, and S. P. Carter (2015b), Rupture speed dependence on initial stress profiles: Insights from glacier and laboratory stick-slip, *Earth Planet. Sci. Lett.*, *411*, 112–120, doi:10.1016/j.epsl.2014.11.025.
West, M. E., C. F. Larsen, M. Truffer, S. O'Neel, and L. LeBlanc (2010), Glacier microseismicity, *Geology*, *38*(4), 319–322.
Winberry, J. P., and S. Anandakrishnan (2009), Seismic observations of transient subglacial water-flow beneath MacAyeal Ice Stream, West Antarctica, *Geophys. Res. Lett.*, *36*, L11502, doi:10.1029/2009GL037730.
Zhu, L., and L. A. Rivera (2002), A note on the dynamic and static displacements from a point source in multilayered media, *Geophys. J. Int.*, *148*, 619–627, doi:10.1046/j.1365-246X.2002.01610.x.
Zoet, L. K., S. Anandakrishnan, R. B. Alley, A. A. Nyblade, and D. A. Wiens (2012), Motion of an Antarctic glacier by repeated tidally modulated earthquakes, *Nat. Geosci.*, *5*(9), 623–626, doi:10.1038/ngeo1555.
Zwally, H. J., W. Abdalati, T. Herring, K. Larson, and J. Saba (2002), Surface melt-induced acceleration of Greenland ice-sheet flow, *Science*, *297*(5579), 218–222, doi:10.1126/science.1072708.